Poly(vinyl alcohol)/oxidized cellulose nanofibril composite films with high nanofiller content for enhanced packaging applications

Khadija Trigui, Albert Magnin, Jean-Luc Putaux, Sami Boufi

Poly(vinyl alcohol)/oxidized cellulose nanofibril composite films with high nanofiller content for enhanced packaging applications

Khadija Trigui[a,b], Albert Magnin[b,*], Jean-Luc Putaux[c], Sami Boufi[a,*]

[a] *University of Sfax - LMSE - Faculty of Science - BP 802 - 3018 Sfax, Tunisia*

[b] *Univ. Grenoble Alpes, CNRS, Grenoble INP, LRP, F-38000 Grenoble, France*

[c] *Univ. Grenoble Alpes, CNRS, CERMAV, F-38000 Grenoble, France*

* Corresponding authors:

albert.magnin@univ-grenoble-alpes.fr

sami.boufi@fss.rnu.tn

Published in: **Journal of Industrial and Engineering Chemistry** *113* (2025), 602-613

DOI: 10.1016/j.jiec.2025.01.016

ABSTRACT

The performance of poly(vinyl alcohol) (PVA) thin composite films incorporating 10-90 wt% cellulose nanofibrils (CNFs) prepared by TEMPO-mediated or periodate oxidation (T-CNFs and P-CNFs, respectively) was evaluated. The tensile strength and Young's modulus significantly increased with increasing CNF content, while the elongation at break decreased. Differential scanning calorimetry revealed that the crystallization of PVA was inhibited by over 50 wt% T-CNFs and 30 wt% P-CNFs. PVA/T-CNF films lacked barrier properties without additional compression, while PVA/P-CNF films exhibited barrier capabilities without post-pressure treatment, which was attributed to the shorter P-CNFs. Oxygen transmission rate tests confirmed that the barrier properties were preserved up to 50 wt% CNFs, correlating with the inhibition of PVA crystallization, while the film transparency increased with increasing CNF content. Aqueous PVA/CNF suspensions with a high CNF content can thus be used as thin layers on polymer or paper-based substrates to enhance their barrier properties, mechanical strength, and thermomechanical stability, with applications in environmentally friendly packaging.

1. Introduction

Poly(vinyl alcohol) (PVA) and nanocellulose (NC) have gained attention in the field of packaging due to their unique properties and potential for sustainability [1-3]. PVA, most specifically in its fully hydrolyzed grade, offers a combination of water solubility, film-forming ability, adhesive properties, biocompatibility, high transparency, biodegradability, and chemical resistance, making it a valuable polymer for packaging applications using conventional film-forming techniques such as casting, coating, or extrusion [4]. Cellulose nanofibrils (CNFs), derived from cellulose fibers, are known for their exceptional mechanical properties, including high tensile strength and stiffness. They can reinforce PVA matrices, giving rise to sustainable and functional packaging films with improved strength, barrier, and biodegradation properties. PVA exhibits good barrier properties against gases, making it suitable for food packaging applications where oxygen and moisture barriers are necessary to prolong shelf life. The addition of NC is expected to further enhance the barrier effect against oxygen, moisture, and other gases, promoting the development of fully biodegradable composite materials with improved mechanical, barrier, and durability performance [5,6].

Numerous works reported on composites based on PVA and NC [6-10]. However, in most of these works, the NC content was lower than 15 wt%, and, to our knowledge, only two studies have reported on the use of more than 50 wt% CNFs in PVA. In the first one, CNFs were isolated from sugar beet chips by high-pressure homogenization (HPH). The PVA/CNF composite exhibited significantly better mechanical performance compared to PVA alone [11]. In the second study, CNFs were obtained from paper pulp by combining mechanical grinding and HPH. The incorporation of CNFs improved the crystallinity, mechanical strength, Young's modulus, glass transition temperature (T_g), and thermal stability of PVA matrices [12].

In all reported works, the addition of NC enhanced the mechanical performance in terms of stiffness and strength. This effect was explained by the set-up of entangled and percolated networks for CNFs or cellulose nanocrystals (CNCs) when the content exceeded a critical threshold. However, given the relatively high glass transition temperature (T_g) of PVA (50-70 °C), depending on the water content of the PVA films), the increment in stiffness and strength with NC lower than 15 wt% remained modest compared to a ductile matrix with a T_g below 0 °C. For instance, at 10 wt% CNCs, the increment in tensile modulus and strength rarely exceeded twice that of the neat PVA matrix, which justifies the interest in further increasing the NC content in PVA above 20 wt%. Given the water solubility of PVA, the preparation of composites with a high NC loading should not be a problem from the processing point of view. The main data on the mechanical pressing of PVA/CNF composites with different CNF contents were collected in **Table 1** [13-17].

NC may be used as an additive to reduce the water sensitivity of PVA by favoring its crosslinking and consuming a fraction of its hydroxyl groups via specific functionalization. In this sense, the use of dialdehyde-functionalized CNFs (DalCNFs) prepared via periodate oxidation was shown to reduce the hydrophilicity of PVA films and improve their water resistance. However, the NC content did not exceed 5 wt%. In another approach, silane-modified CNFs were used as dual reinforcement and crosslinking agents in PVA matrices [18]. The chemical crosslinking between CNFs and PVA consumed a fraction of the hydroxyl groups, resulting in a marked increase in water resistance, a decrease in hydrophilicity, and better mechanical properties.

Table 1: Mechanical properties of pure PVA and PVA/CNF composite films.

Film	Young's modulu (MPa)	Elongation at break (%)	Tensile strengt (MPa)	Type of CNFs	Reference
PVA	248	331	34.1	Daicel Chemical Industries, Japan	[15]
PVA + 10 wt% CNFs	1033	25.2	53.2		
PVA	522	-	34.5	Rice straw and high-pressure homogenizatic	[16
PVA + 3 wt% CNFs	707	-	50.8		
PVA	380	-	37	Kraft pulp by a mechanical process	[17]
PVA + 10 wt% CNFs	540	-	60		
PVA + 6 wt% CNFs	-	371.7	25.31	CNFs by TEMPO oxidation	[18]
PVA	-	148	48	Rice straw, TEMPO oxidation end steam explosion	[19]
PVA + 5 wt% CNFs	-	85	40		
PVA	250	22.7	17	Sugar beet chips and high-pressure homogenization	[10]
PVA + 50 wt% CNFs	5300	1.6	61		
PVA	164	19.1	29.7	Paper pulp grinding an high-pressure homogenization	[11]
PVA + 60 wt% CNFs	1022	247.8	55.6		

The applicability of PVA/NC as a coating formulation for high-barrier packaging applications was also successfully tested for poly(lactic acid) (PLA) and polypropylene (PP). A PVA and dialdehyde-modified NCs (DalNCs) mixture was coated onto PLA films using a doctor blade [19]. The resulting films exhibited high gas barrier performance, attributed to the crosslinking of DalNCs and PVA. PVA/CNC coatings were also applied to PP films. The barrier performance to oxygen (96 %) and carbon dioxide (90 %) was improved when compared to a pure PP substrate while maintaining a lower water sensitivity [20]. A similar strategy may be applied to paper-based packaging.

In the present study, the performance in terms of mechanical, thermal, optical, structural, and barrier properties of PVA thin composite films incorporating two types of NCs, namely CNFs prepared by TEMPO-mediated or periodate oxidation (T-CNFs and P-CNFs, respectively) was investigated. These types of CNFs were specifically selected due to the presence of different functional groups. The aldehyde and the carboxylic groups generated by the chemical modification were meant to improve their reactivity and compatibility with PVA, resulting in better dispersion and stronger interfacial interactions, which is crucial for the performance of the composite. For T-CNFs, the disintegration was performed by twin-screw extrusion in the presence of PVA, while for P-CNFs, a gel was obtained after the oxidation treatment, without using any additional TSE. The composites based on T-CNFs and P-CNFs with a CNF content from 10 to 90 wt% were prepared by casting. The main objective was to study how the presence of NC at a high content induced a change in the properties of the PVA/NC thin films. Unlike most of the previously reported works on PVA/NC composites where the NC content barely exceeded 10 wt%, in the present work, a high NC loading was used to increase the biobased content as much as possible, for potential application as a barrier and tough coating layer in polymers, and paper- or board-based packaging.

2. Experimental section

2.1. Materials

Never-dried eucalyptus pulp (NDP) from Torraspapel with a 50 wt% water content was used as a source of cellulose fibers to prepare CNFs. The 2,2,6,6-tetramethylpiperidine-1-oxyl radical (TEMPO), sodium bromide (NaBr), sodium (meta)periodate ($NaIO_4$), and PVA (Mowiol 20-98) were purchased from Sigma Aldrich. The degree of hydrolysis of PVA was 98 %, and its molecular weight was 125000 g mol^{-1}. PVA solutions were prepared at 1 and 15 wt% by slowly dissolving PVA powder in distilled water under constant stirring at 90 °C for 2 h. The sodium hypochlorite (NaClO) solution was a commercial product with a ClO^- concentration of about 2.7 %, as determined by volumetric titration with sodium thiosulfate.

2.2. TEMPO/NaClO/NaBr and periodate oxidation

The processing conditions were selected from our previous results regarding the preparation of PVA/CNF suspensions with a high solid content and good fibrillation, using twin-screw extrusion [21]. Cellulose fibers were oxidized using the TEMPO/NaClO/NaBr system under basic pH conditions. Briefly, fibers (10 g) were dispersed in water (1 L) containing the TEMPO radical (50 mg/g fibers) and NaBr (0.2 g/g fibers). The suspension was stirred at 4-5 °C while the hypochlorite solution was continuously added dropwise during 1.5-2 h and the pH was kept around 10 by the addition of a 0.1 M NaOH. The oxidized fibers were recovered by filtration and multiple

washing cycles to pH neutrality. The carboxyl content was measured by conductimetric titration as described in our previous work [22]. Never-dried pulp (2.5 g) was mixed with 200 mL of water, then 4.3 g of $NaIO_4$ was added, and the reaction vessel was covered with aluminum foil to prevent periodate decomposition. The reaction mixture was magnetically stirred in a water bath at 40 °C for 48 h. The product was then filtered and washed several times with deionized water to remove iodine-containing compounds. The aldehyde content was determined using an oxime reaction.

2.3. Twin-screw extrusion of fibers

The PVA/oxidized fiber mixtures were extruded in a pilot-scale Letsritz 18 MAXX co-rotating twin-screw extruder (screw diameter D = 18.5 mm and length 32D (60 cm) (**Fig. S1A**). The kneading element was composed of the standard element in 30, 45, 60, and 90° designs to ensure the highest shearing effect. Oxidized fibers (200 g) with a solid content (SC) of 30 wt% were mixed manually with the PVA aqueous solution at 15 wt% so that the PVA/CNC weight ratio based on dry material was 20/80, and the solid content of the total mixture was around 25 wt%. The mixture was fed into the extruder and processed at 25 °C at a screw-speed of 200 rpm during 5 passes to ensure effective fibrillation, with a residence time of the fiber during each pass of about 1 min. At the exit of the extruder, the mixture was in the form of a strand having a thick gel consistency (**Fig. S1B**). The nanosized fraction (NF) was determined by gravimetry after centrifugation following the methodology reported elsewhere [23].

2.4. Preparation of PVA/CNF composite films

PVA/CNF composites were prepared with a CNF content between 10 and 90 wt%. For the extruded fibers, an appropriate amount of PVA/CNF was mixed, diluted to 3 % and the mixture was stirred for 1 min with a vortex, followed by a 3-min sonication at a 70 % power amplitude using a 20 kHz frequency sonicator (Sonics Vibracel Model CV33) with a 25 mm diameter horn and a power of 400 W. Periodate oxidized fibers were mixed with the appropriate amount of PVA solution, and treated as previously described. The mixtures were dried at 40 °C for 24 h in a conventional oven to form the films. The thickness of the PVA composite films was *ca.* 40 ± 3 µm. Some dried films were thermocompressed at 8 bar and 80 °C for 3 min. No notable variation in film thickness was observed. A scheme summarizing the sequences to produce CNFs and PVA/CNF composites is given in **Fig. S2**.

2.5. Microscopy

Drops of fiber or CNF suspensions (*ca.* 0.05 % w/v) were observed with a Zeiss Axio microscope equipped with an AxioCamMRc5 digital camera. The PVA/CNF films were fractured in liquid nitrogen. The fracture surfaces were coated with Au/Pd in a Safematic CCU-010-HV sputter-coater and observed in a Thermo Scientific FEI Quanta FEG 250 scanning electron

microscope (SEM) operating at 2.5 kV. Droplets of dilute CNF suspensions (*ca.* 0.001 wt%) were deposited onto freshly glow-discharged carbon-coated grids and negatively stained with 2 wt% uranyl acetate. The specimens were observed with a JEOL JEM 2100-Plus transmission electron microscope (TEM) operating at 200 kV. Images were recorded with a Gatan Rio 16 digital camera.

2.6. X-Ray diffraction (XRD) and Fourier-transform infrared (FTIR) spectroscopy

Fragments of PVA/CNF composite films were cut, fixed onto a collimator, and X-rayed under vacuum with a Philips PW3630 generator operating at 30 kV and 20 mA (Ni-filtered CuKα beam, $\lambda = 0.1542$ nm). Two-dimensional XRD patterns recorded on Fujifilm image plates and read in a Fujifilm BAS1800-II bioanalyzer were converted into diffraction profiles by rotational averaging and normalized to the total amount of material between 10 and 37°. FT-IR spectra of the films were recorded on a Perkin-Elmer Spectrum spectrometer equipped with a diamond ATR accessory. Ten scans were run from 4000 to 600 cm^{-1} wavenumbers.

2.7. Turbidity measurements and transmittance

The turbidity of dilute PVA/CNF suspensions. (0.2 wt%) was measured with an AL450T-IR 1100 NTU turbidimeter (5 measurements per sample). The optical properties of the composite films were evaluated using a UV-Vis Lambda 35 spectrometer (Perkin Elmer, USA), measuring the transmittance between 800 and 400 nm.

2.8. Contact angle

Contact angles were measured by depositing a calibrated drop of water on the film and continuously measuring the shape of the drop using a Dataphysics OCA 15 analyzer, fitted with a high-resolution CCD camera with an acquisition speed of 50 images per second.

2.9. Mechanical properties

Tensile tests were performed on rectangular films of 40 μm thickness (20 mm × 5 mm), using an ARES G2 rheometer (TA Instruments) at a speed of 10 mm min^{-1}. Samples were stored for 2 days in a room maintaining a temperature of 25 °C and a relative humidity (RH) of 50 % checked with a humidity meter placed in the room. Five tests were conducted for each sample. Dynamic mechanical analysis (DMA) tests were run using a PYRIS Diamond analyzer (Perkin-Elmer, Waltham), at a heating rate of 2 °C min^{-1} and a temperature ranging from -20 to 140 °C under air and nitrogen sweep at 1 Hz.

2.10. Barrier properties to water and oxygen

The water vapor transmission rate (WVTR) that indicates the amount of water vapor that passes through the sample per unit area per unit time was determined according to the ISO 2528 standard. Samples were placed on dishes containing anhydrous $CaCl_2$ salt that were hermetically

sealed with wax and stored at 23 °C and 50 % RH. The oxygen transmission rate (OTR) was measured using the M8001 analyzer according to the ISO 15105 standard. One side of the sample was exposed to an oxygen flow, and the amount of oxygen diffusing through the tested material was measured by the oxygen detector. At least two replicates were analyzed over a 3-5 cm^2 areas depending on the available samples.

2.11. Thermal properties

Differential scanning calorimetry (DSC) thermograms were recorded under nitrogen using a Perkin-Elmer DSC-4000 calorimeter. Samples of approximately 5-10 mg were hermetically sealed in an aluminum pan, heated from 10 to 240 °C at a heating rate of 10 °C min^{-1} (first heating), kept for 1 min, cooled to 20 at 10 °C min^{-1}, and reheated to 240 °C. The degree of crystallinity X_c was calculated using **Eq. 1**:

$$X_c = \frac{\Delta H_m}{\Delta H^0 \mathrm{m} \times w_{\mathrm{PVA}}} \quad \textbf{(1)}$$

where ΔH_m is the melting enthalpy, $\Delta H°_m$ is the theoretical melting enthalpy of 100 % crystalline PVA (161 J g^{-1}), and W_{PVA} is the weight fraction of PVA in the composite. The thermal degradation of the composite films was analyzed in Perkin Elmer TGA 400 thermogravimetric analyzer). A sample of approximately 5-10 mg was weighed and heated under dry air from 20 to 800 °C at a heating rate of 10 °C min^{-1}.

3. Results and discussion

3.1. Characterization of PVA/CNF suspensions

The extrusion of PVA/T-CNF was achieved at a 25 wt% content, giving at the exit of the dye a continuous filament, turning more gelatinous with an increasing number of passes through the TSE. Then, the extruded gel was diluted to 3 wt% and sonicated for 3-min resulting in a consistent translucent gel that was used to prepare the films. The periodate-oxidized fibers could not be extruded, as a gel-like material was obtained after oxidation. The gel was sonicated to further enhance the efficiency of fiber disintegration into NC. An optical micrograph image of the neat fibers at a similar concentration is given in **Fig. S3**. The extruded-sonicated T-CNFs and P-CNFs only contained a minor fraction of micron-scale swollen fibers. In T-CNFs, residual fibers exhibited balloon-like swollen regions that were explained by the radial expansion of cellulose in the secondary wall, causing the burst of the primary wall (**Fig. 1A** and **1B**). In P-CNFs, the residual fibers exhibited swollen regions with loose cohesion due to the oxidation treatment, as explained in our previous work (**Fig. 1C** and **1D**) [21].

The supernatants of dilute T-CNF and P-CNF suspensions were observed by TEM. T-CNFs and P-CNFs exhibited different morphologies. T-CNFs contained individual long entangled

nanofibrils, in addition to bundles of fibrils that were not fully individualized by the disintegration treatment (**Fig. 1E** and **1F**). This morphology agrees with our previous work where a labscale microcompounder with different screw characteristics was used for TSE [21]. In the DSM microcompounder, the two screws were arranged in a conical shape, tapering towards the discharge end of the extruder, while in the pilot TSE, the screw encompasses a combination of conveying elements and kneading disks in which each disc is offset by a given angle from the previous disc ensuring high localized shear rates in these zones. This later screw configuration ensured a better shearing effect combined with a high compression rate in the kneading block, to enhance the disintegration of the fibers during the extrusion process.

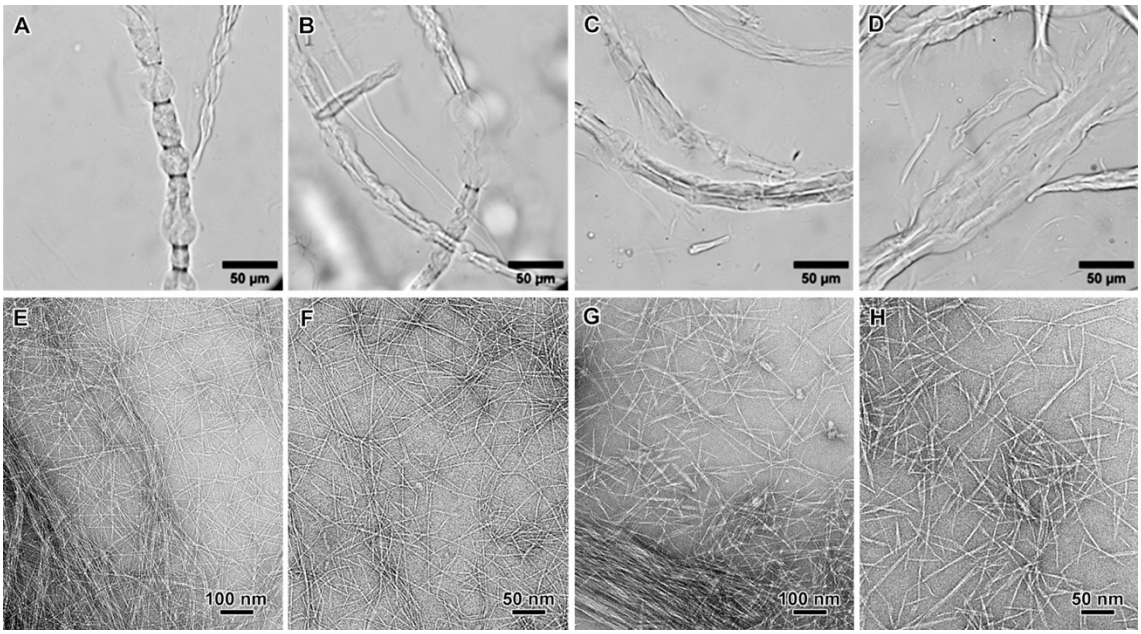

Fig. 1. Optical micrographs of T-CNFs (A,B) and P-CNFs (C,D), and corresponding TEM images of negatively stained suspensions of T-CNFs (E,F) and P-CNFs (G,H).

The P-CNF fraction also contained swollen fragments of fibers incompletely exfoliated by the disintegration treatment (**Fig. 1G)**. In the supernatant, P-CNFs were significantly kinked, presumably due to the high degree of oxidation and preferential but incomplete action of the oxidant on the disorganized regions of CNFs (**Fig. 1H**) [24]. Indeed, the shape and size of the straight segments were fairly similar to those of CNCs from the same source of cellulose [24]. The turbidity of T-CNFs and P-CNFs was 32 and 22.4 NTU, respectively, which is quite low, supporting the efficient disintegration of treated fibers into CNFs. This was further confirmed by using centrifugation, with a fibrillation yield higher than 90 % and with a higher degree for P-CNFs **(Table S1)**.

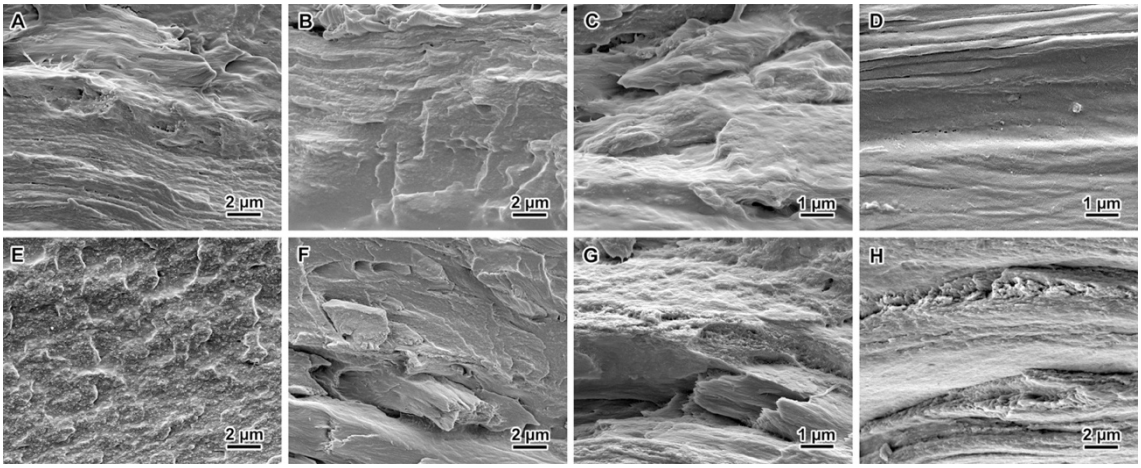

Fig. 2. SEM images of cross-section fractured surfaces of PVA/T-CNF films with 20 wt% (A), 30 wt% (B), 50 wt% (C), and 80 wt% (D) T-CNFs, and PVA/P-CNF films with 20 wt% (E), 40 wt% (F), 50 wt% (G) and 80 wt% (H) P-CNFs.

3.2. Morphology of PVA/CNF composite films

The cross-sections of cryofractured PVA/CNF composite films were observed by SEM. A homogeneous and defect-free interface was observed in the 100 % PVA film (**Fig. 2A**). The images of the PVA/CNF films revealed the compact layered structure usually observed in CNF nanopapers without the addition of polymer [21,25]. The layered structure was not well resolved for all compositions, presumably due to the presence of the PVA matrix acting as a binder between the CNF layers. The presence of micropores was not detected from the SEM images. However, low-magnification views of the cross-section of the films (not shown) revealed the presence of several micron-scale fibers, which may be the origin of the sharp decrease in the barrier properties to O_2 and H_2O observed over a critical CNF content.

In the literature, the presence of this layered structure was attributed to aggregation and flocculation during the final water evaporation in nanopaper production by casting [26]. This structure was observed for both T-CNFs and P-CNFs. At higher magnification, the fracture surfaces of PVA/T-CNF and PVA/P-CNF films were much rougher than those of pure PVA. This is due to the incorporation of CNFs into the polymer matrix, and, presumably, to the presence of incompletely disintegrated fragments of fibers [27,28]. Furthermore, the images showed that both types of CNFs were compatible with PVA. No phase separation or cavity formation at the interfaces was observed, which is likely promoted by the high affinity between PVA polymer and CNFs, thanks to the set-up of hydrogen interaction between surface hydroxyl groups of CNFs and PVA.

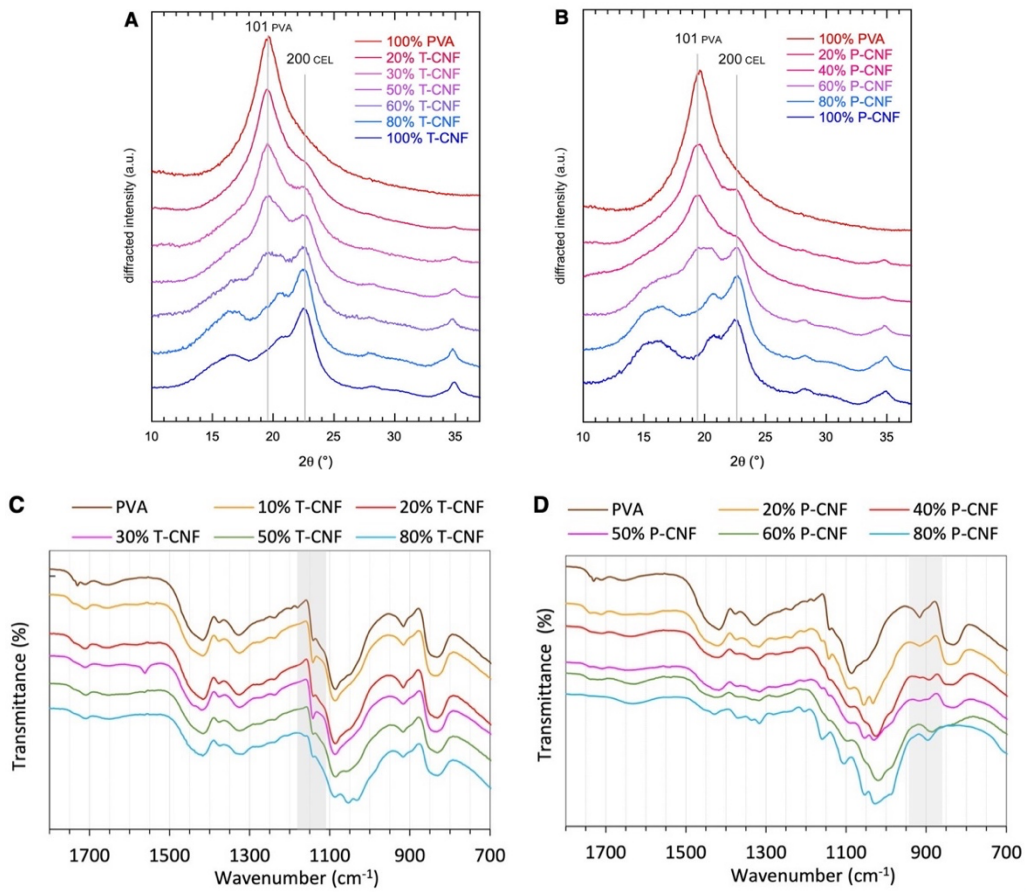

Fig. 3. XRD profiles of PVA/T-CNF (A) and PVA/P-CNF (B) films with different CNF contents. The main peaks of PVA (101) and cellulose (200), respectively, are indicated by vertical lines. (C,D) FTIR spectra of the corresponding composites.

3.3. Structure of PVA/CNF composites

The XRD profile of pure PVA was characterized by a broad diffraction peak around 19.8° attributed to the (101) crystallographic planes, confirming its semicrystalline structure [29] (**Fig. 3A**). The profiles of T-CNF and P-CNF films (**Fig. 3A** and **3B**) contained the diffraction peaks of cellulose I. According to the indexing of the Iβ allomorph, the broad peak centered around 2θ = 16.2° corresponds to the overlap of the $1\bar{1}0$ and 110 reflections, while the peaks at 22.4 and 34.6° correspond to the (200) and (004) lattice planes, respectively [30]. The profiles of the PVA/CNF films exhibited the peaks of cellulose I and PVA for compositions containing less than 50 wt% CNFs. Beyond this content, the peak of PVA became less pronounced with the increase in CNF content, and beyond 80 wt%, the peaks were no longer visible. This result suggested a decrease in the crystallinity of PVA with the incorporation of CNFs.

The FTIR spectrum of PVA/CNF composites (**Fig. 3C** and **3D**) showed the characteristic absorption bands of PVA are at 1416 cm^{-1} (CH_2 bending), 1325 cm^{-1} (δ (OH), rocking with CH wagging), 1140 cm^{-1} (shoulder stretching of C-O) (crystalline sequence of PVA), 1080 cm^{-1} (stretching of C-O and bending of OH) (amorphous sequence of PVA), 920 cm^{-1} (CH_2 rocking),

825 cm^{-1} (C-C stretching) [31]. The typical bands of CNF are those of cellulose at 890 cm^{-1} (C−H deformation vibrations), 1020 and 1050 cm^{-1} (C−O stretching), 1110 and 1155 cm^{-1} (C−O−C ring-stretching vibration, 1325 cm^{-1} (C−H_2 wagging), 1366 cm^{-1} (C−H bending), and 1421 cm^{-1} (C−H_2 symmetric bending). In PVA/T-CNF composites, the FTIR bands of PVA and cellulose remained nearly unchanged, except for the band at 1140 cm^{-1}, which decreased as the CNF content increased. This evolution was due to the decrease in the PVA crystallinity degree. For PVA/P-CNF (**Fig. 3D**), in addition to the decrease in intensity of the band at 1140 cm^{-1}, a new weak band around 880-900 cm^{-1} is seen, accompanied by a decrease in the intensity of the band at 920 cm^{-1}. This new band corresponds to the hemiacetal groups resulting from the condensation of the aldehyde of P-CNFs with hydroxyl groups of PVA. The emergence of these groups supports the hypothesis of the formation of hemiacetal bonds between the aldehyde groups of P-CNFs and hydroxyl groups of PVA [24]. To the best of our knowledge, the only work that reported the formation of hemiacetal bonds between aldehyde groups and hydroxyl groups was conducted with PVA/starch systems [32]. While this specific reaction mechanism has not been widely reported with PVA, we believe that the same principles can be applied to our system due to the similar chemical groups involved.

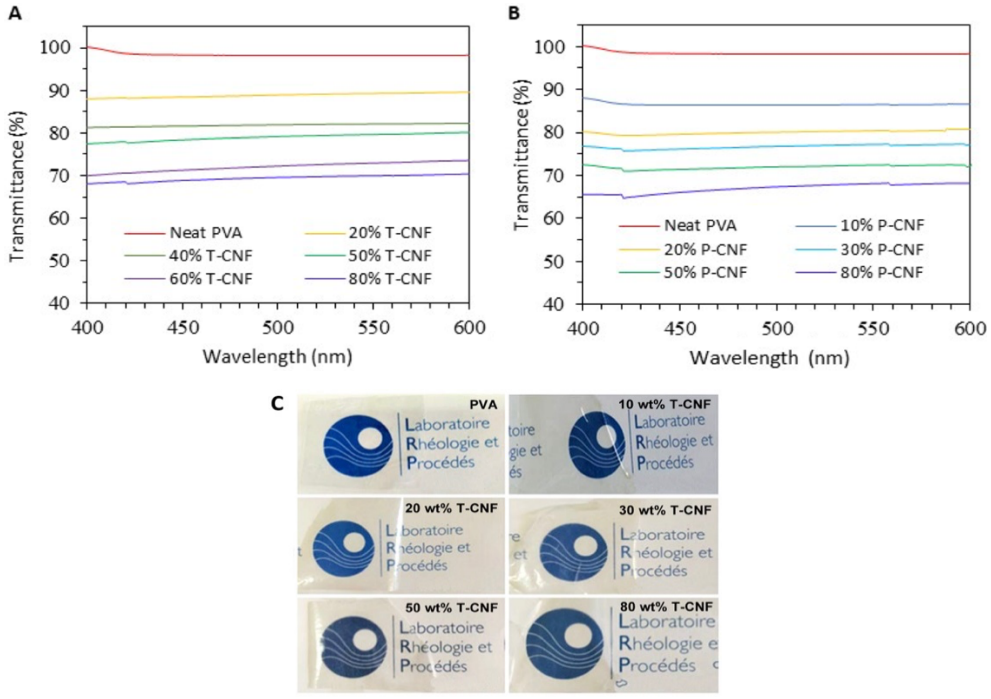

Fig. 4. Transmittance curves of composite films as a function of the CNF content: A) PVA/T-CNF, B) PVA/P-CNF; C) photos of PVA/T-CNF films.

3.4. Optical properties of PVA/CNF films

The photographs shown in **Fig. 4** and the transmittance Tr of PVA/CNF films allowed evaluating the transparency of the composites. Various factors, such as particle size,

agglomeration, phase separation, etc., influence the overall transparency of the system. As illustrated in **Fig. 4A** and **4B**, the 100 % PVA film exhibits extremely high transparency and clarity, as evidenced by a Tr higher than 95 %. However, Tr gradually decreased with the addition of CNF. For T-CNFs, Tr was around 65 % for the film that contained 80 wt% T-CNFs. The PVA/P-CNF transmittance followed the same trend (**Fig. 4B**), with a gradual decrease in transmittance as the CNF content increases, and transmittance values remaining above 65 wt% up to 80 wt% CNFs.

This decrease in film transparency is likely due to light scattering caused by the presence of CNFs. The light scattering through a film is controlled by both the refractive index difference between the present phases and the size of the dispersed objects. The refractive indices of PVA and cellulose are 1.52 and 1.47, respectively. This difference accounts for the refraction and reflection effects experienced by light passing through the composite film. However, the size of the dispersed objects also notably affects the intensity, with a dependence on D^3 (D: diameter of the objects), implying that larger objects induce a marked decrease in transmittance. For objects with a square section smaller than approximately 50 nm, light scattering effects become minimal, and the presence of particles does not affect the film transparency, provided there is good dispersion. Therefore, the decrease in Tr with an increase in CNF content is likely due to the presence of non-fibrillated fiber fragments or CNF aggregates.

3.5. Thermal transitions in PVA/CNF composite films

The impact of CNFs on the thermal transition of the PVA matrix was investigated by DSC. The second-scan DSC thermograms for PVA/T-CNF and PVA/P-CNF shown in **Figs. 5** and **S4** revealed a glass transition at T_g characterized by abrupt change of the slope of the DSC thermogram and a melting peak (T_m). For the neat PVA, the T_g and T_m were located around 80 and 220 °C, respectively, and the cooling scan (**Fig. 5D**) showed a crystallization peak at T_c = 184 °C, and a T_g at the same position. The value of T_g from DSC differed from that determined by DMA, likely because the T_g measured by DMA is that of the film containing some moisture which acts as a plasticizer for PVA. However, in DSC, T_g is that of PVA without water, which was removed during the first scan.

In the presence of T-CNFs, a shift of T_m to a lower temperature with a decrease in the area of the melting peak was observed, and the melting peak disappeared over 50 wt% CNFs. The same tendency was observed for the crystallization peak (**Fig. 5B**). The T_g did not significantly change with the addition of CNFs that hampered the crystallization of the PVA matrix, which was more clearly seen from the evolution of the crystallinity degree X_c *vs.* CNF content (**Fig. 4C**). A similar tendency was observed for P-CNFs (**Fig. S4**), with a more pronounced effect, as the total disappearance of the melting peak appeared over 40 wt% CNFs.

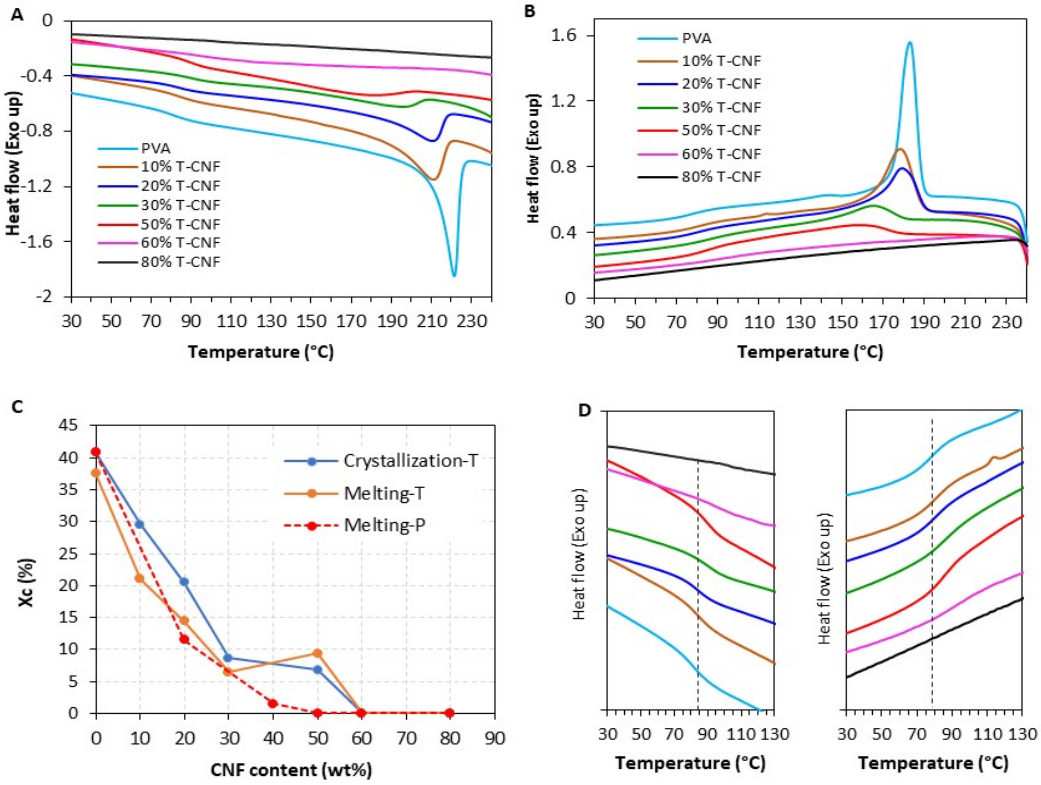

Fig. 5. DSC thermograms: (A) first heating; (B) cooling of PVA/T-CNF films at different CNF contents; (C) evolution of the crystallinity rate as a function of CNFs, and (D) magnification of the T_g area in each thermogram.

At 50 wt% T-CNFs, the X_c value was nearly similar to that at 40 wt% T-CNFs when considering the melting process, but it was lower than that of 40 wt% T-CNFs when considering the crystallization after melting. This apparent discrepancy is likely due to an anomaly during film drying. The X_c value determined from the crystallization during cooling is considered to be more accurate since the thermal history is erased after melting. The decrease in PVA crystallization has been reported in the case of CNCs [33,34]. However, the CNC content was below 25 wt%, and only a decrease in crystallinity degree was reported. The hampering of the crystallization of PVA when NC was added was presumably related to the specific structure of PVA, in particular its ability to form hydrogen bonds with the surface hydroxyl groups of NC. This interaction limits the mobility of the chains and opposes the assembly of PVA chains into a crystalline network. It is worth mentioning that the opposite trend was observed when nanocelluloses were incorporated in a semicrystalline polymer matrix with a low polarity, such as PLA [35], PP, and PHB, where the presence of nanocellulose, on the contrary, enhanced the crystallization by acting as a nucleating agent.

The more pronounced effect on hampering the crystallization of PVA when P-CNFs were added (**Fig. S4**) is likely due to the presence of aldehyde groups in the P-CNFs that can react with a hydroxyl group, producing a hemiacetal. Accordingly, the reaction between the hydroxyl groups

of PVA and aldehyde groups of P-CNFs probably took place, at least partially, after the complete removal of water. The occurrence of this reaction could explain the significant impact of P-CNFs in inhibiting the crystallization of PVA. The reaction between P-CNFs and PVA would likely promote crosslinking, contributing to improved stiffness, strength, and water resistance. However, additional studies are needed to investigate how the aldehyde groups in P-CNFs might impact the long-term properties of the film.

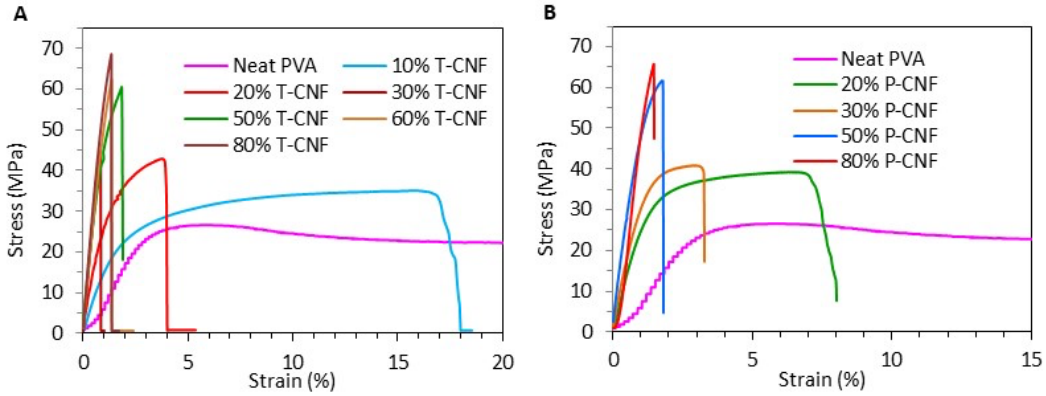

Fig. 6. Tensile test curves of PVA/T-CNF (A), and PVA/P-CNF (B) films at different T-CNF and P-CNF contents.

3.6. Mechanical properties of PVA/CNF composites

The mechanical properties of composites PVA/CNF films incorporating 10 to 80 wt% CNFs were investigated by tensile tests and DMA. The tensile test traces of T-CNFs and P-CNFs are shown in **Fig. 6**, from which the tensile modulus (E), the strength (σ), and the elongation at break (ε) were calculated. The decrease in elongation at break was associated with the rigid structure of the CNF network that limited the mobility of the PVA chains. E/σ steadily increased with increasing CNF content, with a nearly similar tendency for T-CNFs and P-CNFs. For instance, the E/σ increased from about 0.5 GPa/32 MPA for neat PVA film to 6.5 GPa/67, and 6.7 GPa/66 MPa, in the presence of 80 wt% T-CNFs and P-CNFs, respectively. The enhancement of the strength and stiffness was expected and in line with the strong reinforcing potential of NCs in PVA, even at a low content [36-39]. This significant reinforcing effect of CNFs was due to their high aspect ratio, high stiffness, and their aptitude to form entangled cohesive networks held by hydrogen bonds.

The percolation and Halpin-Tsai (HT) models were explored to fit the evolution of the tensile modulus E and strength σ with the T-CNF content (**Fig. 7A**). The percolation model is well adapted for NC-based composites, but often at a nanofiller content lower than 15 wt%, while the HT is

mostly adopted for short-fiber composites over a wide range of filler content [40,41]. The percolation model assumes a homogeneous distribution and dispersion of fibers, a perfect fiber/matrix interaction, and an effective interaction between the filler that form a rigid network, held by strong interparticle hydrogen bonds. The set-up of the percolation takes place over a critical percolation concentration [42,43]. The tensile modulus E_c is a function of the volume fraction of the percolating network ψ, the total volume fraction of the nanofiller ϕ:

$$E_c = \frac{(1-2\psi+\psi\phi)E_s E_n + (1-\phi)\psi E_n^2}{(1-\phi)E_n + (\phi-\psi)E_s} \quad \textbf{(2)}$$

where E_s and E_n are the moduli of the NC network and the matrix, respectively. E_r, which differs from that of isolated CNFs, was estimated from the DMA analysis of casted NC films.

$\psi = 0$ when $\phi < \phi_p$ and $\psi = \phi\left(\frac{\phi-\phi_p}{1-\phi_p}\right)^b$ for $\phi \geq \phi_p$ and b = 0.4 for a 3D network. The percolation threshold was estimated by **Eq. 3** [44]:

$$\phi_p = \frac{0.7}{L/d} \quad \textbf{(3)}$$

Young's moduli of the composite (E_c) and the matrix (E_m), are related by **Eq. 4**:

$$\frac{E_c}{E_m} = \frac{3}{8}\left(\frac{1+\zeta\eta_L\phi}{1-\eta_L\phi}\right) + \frac{5}{8}\left(\frac{1+2\eta_T\phi}{1-\eta_T\phi}\right) \quad \textbf{(4)}$$

The ξ shape factor depends on the filler geometry and loading direction. η and ξ are:

$$\eta_L = \frac{\left(\frac{E_f}{E_m}\right)-1}{\left(\frac{E_f}{E_m}\right)+\zeta} \quad , \quad \eta_T = \frac{\left(\frac{E_f}{E_m}\right)-1}{\left(\frac{E_f}{E_m}\right)+2} \quad \text{and} \quad \zeta = 2\frac{L}{d} \quad \textbf{(5)}$$

where E and E_m are Young's moduli of the filler and matrix, respectively.

Table 2. Mechanical and morphological data used in the percolation and HT modeling.

Sample	E_m (GPa)	E_r (GPa)	E_f (GPa)	L (nm)	D (nm)
T-CNF	0.8	9	20	400	20
P-CNF	0.8	12	40	200	10

As the E_r of the CNF network and E_f were not available, we tested the two models by selecting limiting values of E_r (9 and 12 GPa) for T-CNFs, and E_f (20 and 40 GPa). These limits were based on literature data and our previous work [45]. Both the percolation and HT models were tested for PVA/T-CNF composites from the data in **Table 2**. The HT model fitted better the E_c up to an NC volume fraction of about 0.4-0.5, which corresponds to a 50- 60 wt% loading (**Fig. 7A**). This result was unusual compared with literature data where the percolation model successfully described the stiffness of CNC or CNF-containing composites [46,47]. Two reasons might account for this

apparent discrepancy: i) the percolation model was used for nanocomposites with much lower filler contents (<15 wt%), and ii) a ductile matrix with a modulus lower than 0.1 GPa was often used. Indeed, it is well known that the reinforcing effect of NCs becomes significant only over the glass transition temperature (T_g), and only a moderate increment in E_c was observed [48]. Presently, a PVA matrix with E_m = 0.7 GPa at 25 °C was used, with T_g around 30-40 °C, which is out of the E_m range previously explored. The better fit of the HT model for PVA/T-CNF composites at high nanofiller content indicates that the reinforcement was mainly driven by the intrinsic modulus of the CNFs: the more rigid the nanofiller, the stronger the reinforcement. Another likely reason is the high CNF content, over-exceeding the percolation threshold, where the intrinsic impact of the CNFs predominates over the network effect.

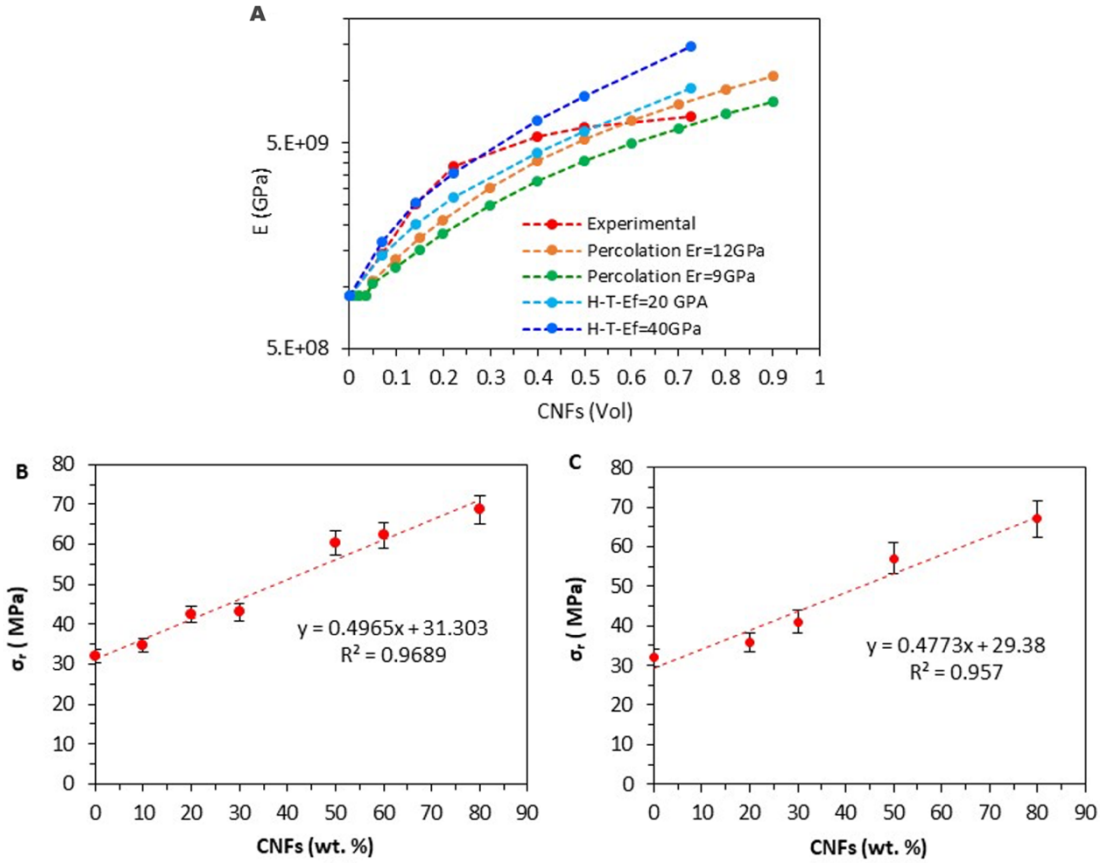

Fig. 7. (A) Evolution of the elastic modulus E (from the tensile plots, the percolation model, and the Halpin-Tsai model) *vs.* CNF content (in vol%); (B,C) evolution of the tensile strength of the composite *vs.* CNF content (wt%) PVA/T-CNF films, (B) for PVA/P-CNF (C) films.

The evolution of the tensile strength of the films $\sigma_r = f(\phi)$ as a function of the CNF content reveals a quasi-linear progression (**Fig. 7B** and **7C**), suggesting that a rule of mixture (ROM) model [49] can be used to predict the strength of fiber-reinforced composites based on the weighted contributions from the filler and the matrix. According to this model, the strength σ_c is expressed as:

$$\sigma_r = \eta_{os}\eta_{ls}\sigma_f V_f + (1 - V_f)\sigma_m \quad (6)$$

where η_o and η_l are the orientation factor and the length factor of the CNFs, respectively, and their product is the efficiency factor of the reinforcement. V_f is the volume fraction of the nanofibers, σ_f, and σ_m represent the tensile strength of the reinforcement and the matrix, respectively. For CNFs laying within the plane, the reinforcement efficiency is expressed as $\eta_{ls} = 1 - l_c/2l$ with $l_c = \sigma_f d/2\tau$ and τ the interfacial resistance between CNFs and the matrix.

The strength of our composite films containing 50 wt% CNFs produced by TSE is similar to that reported by Leitner et al. [11] for PVA/CNF composites, where the CNFs were produced by HPH. A Young modulus of 5.2 GPa, a strength of 61.0 MPa, and an elongation at break of 1.8 % were found [11]. To our knowledge, the present work is the first that explored the properties of PVA/CNF composites over a nanocellulose content from 10 to 80 wt%. Indeed, in most of the literature reports on the use of nanocellulose as a reinforcing agent, the nanocellulose content did not exceed 15 wt%.

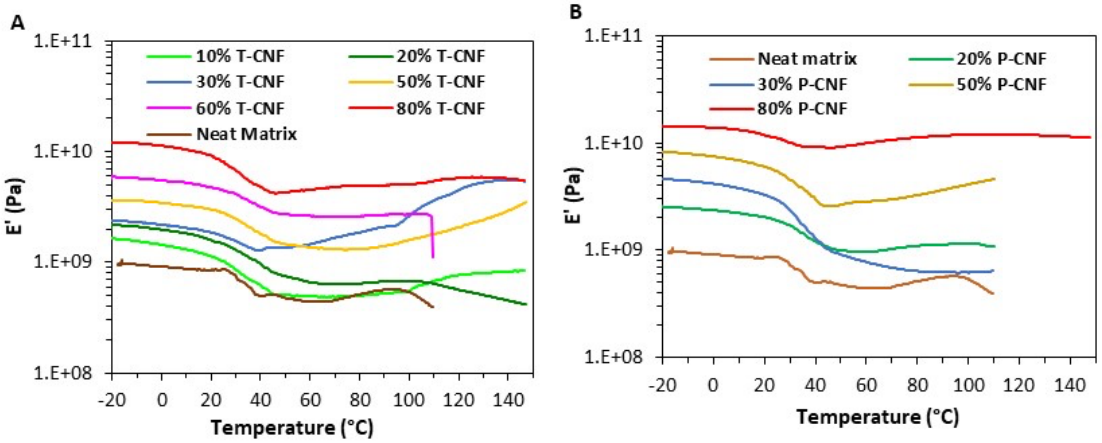

Fig. 8. Evolution of the storage modulus E' as a function of temperature for PVA/T-CNF (A) and PVA/P-CNF (B) films at different CNF contents.

In order to evaluate the evolution of the storage modulus (E′), which reflects the material stiffness, as a function of temperature, a DMA analysis of the composite films was conducted at a temperature ranging from -20 to 140 °C (**Fig. 8**). The neat PVA matrix was characterized by a glassy plateau extending up to 30 °C, with an E′ of *ca.* 1 GPa (**Fig. 8A**). Over this temperature, a decrease in E′ was seen due to the T_g of PVA. However, the polymer stiffness was preserved as evidenced by the modulus of about 0.4 GPa that is stable up to 120 °C, which is likely due to the semicrystallinity of PVA. With the incorporation of CNFs, an upward shift in E′ was observed, indicating an increase in stiffness over the whole temperature domain. For instance, at 80 wt% CNF content, E′ ranged from 10 GPa at the glassy plateau to 5 GPa over T_g which indicates that the

PVA/CNF film kept a high stiffness over a temperature range of -20 to 140 °C. This stiffening effect was explained by the presence of CNFs, as discussed above. A similar tendency was observed for P-CNFs (**Fig. 8B**).

From DMA results, the glass transition occurred at 30 °C, which was lower than the value determined by DSC (around 80 °C). This difference likely results from the fact that in DMA, T_g is that of the films containing some moisture that acts as a plasticizer of PVA, while in DSC, T_g is that of dry PVA, the water having been removed during the first scan.

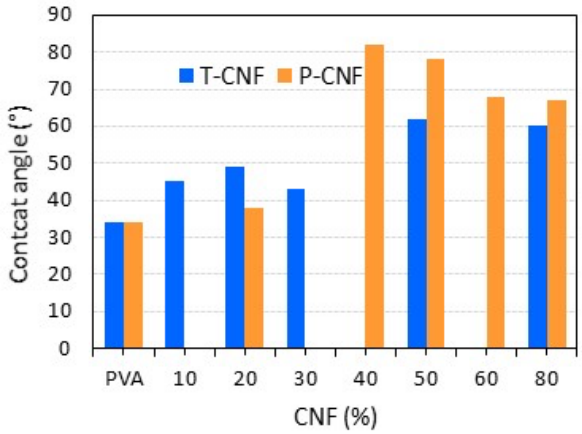

Fig. 9. Evolution of the water contact angle for PVA/T-CNF films and PVA/P-CNF as a function of CNF content.

3.7. Evaluation of the hydrophilic nature of the films

The hydrophilic character of PVA/CNF films was investigated by measuring the contact angle of a water drop deposited on the film *vs.* time (**Fig. S6**), and the evolution of limiting water contact angle was reported in **Fig. 9**. The contact angle of neat PVA film was around 30°, indicating a hydrophilic surface, which was expected given the presence of hydroxyl groups on the PVA structural unit along with the high hydrolysis degree. The contact angle of PVA/CNF films increased to 42-45° for a CNF content up to 30 wt%, and to 60-80° over 40 wt% CNFs, with the highest degree reaching 40 and 50 wt% P-CNFs. The substantial increment in water contact angle over a 40 wt% CNF content indicated a decrease in the hydrophilicity of the film in the presence of CNFs, more significant for P-CNFs. This result was unexpected if we consider that both PVA and CNFs are hydrophilic, given the abundance of the hydroxyl groups on their surface. A possible reason for the higher water contact angle in the presence of CNFs is the mutual interaction through hydrogen bonding between the CNFs and PVA, exposing the hydrophobic backbone of PVA to the surface. A similar tendency was noted in a previous work for PVA/CNC films containing 30-50 wt% CNCs [15]. The more pronounced effect observed with P-CNFs

would be the consumption of a fraction of PVA hydroxyl groups by reaction with the aldehyde groups in P-CNFs, an effect mentioned in the literature for PVA/CNC films containing 30-50 wt% CNCs [20].

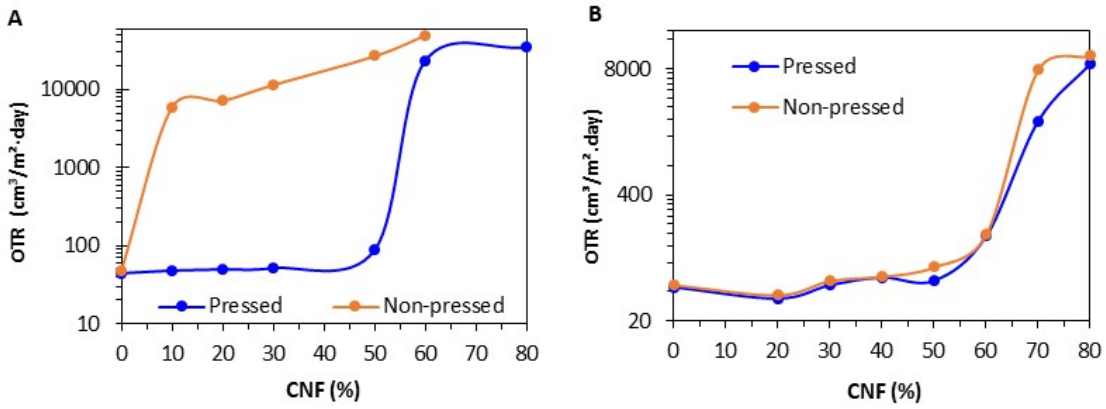

Fig. 10. Evolution of the OTR for PVA/T-CNF (A) and PVA/P-CNF (B) composite films as a function of CNF content for pressed and non-pressed films.

3.8. Barrier properties of PVA/CNF films

The barrier properties of PVA/CNF films as a function of nanofiller content were investigated for both T-CNFs and P-CNFs by measuring the OTR at 0 and 50 % RH. The films were prepared by casting PVA and CNF mixtures at room temperature, and all films had the same thickness of around 40 µm. In addition to the film obtained by casting, pressed/non-pressed films were also characterized. The evolution of OTR for pressed and non-pressed films at different T-CNF and P-CNF contents is shown in **Fig. 10.** The neat PVA film has a relatively low OTR of around 40 cm^3 m^{-2} day^{-1}, which is known for PVA with a high hydrolysis degree of over 98 % [50]. This high barrier against O_2 is due to the strong intermolecular cohesion among PVA chains driven by hydrogen bonding and the crystallinity of PVA. The compression of the film affected the OTR values for T-CNFs, while nearly no effect was noted for P-CNFs. One possible reason for the beneficial effect of compression is the leveling of the film surface and the decrease of surface roughness after the compression of the film. The insensitivity of P-CNFs to the compression treatment may be due to the higher fraction of nanoscale fibrils and their rodlike morphology, reducing the porosity induced by the presence of micron-scale particles. Another likely reason would be the possible chemical interaction between P-CNFs and PVA via hemiacetal linkages that would tighten the structure and increase the film cohesion. In the following, the results will be discussed for pressed films with T-CNFs and non-pressed films with P-CNFs.

For both types of CNFs, the CNF content in the composite film affected the barrier to O_2. The OTR remained roughly constant around 45-50 cm^3 m^{-2} day^{-1} up to 30 wt% T-CNFs, and increased sharply over 50 wt% T-CNFs, indicating a transition from a low to a high permeability of the film (**Fig. 10A-C**). The behavior remained nearly similar at 0 or 50 % RH. A similar tendency was observed for P-CNFs, but the abrupt increase in OTR occurred over 60 wt% CNFs. In addition, the OTR was lower at 50 % RH than 0 % RH (**Fig. S5**). The gas transport process through non-porous polymers is generally described as a sequence of four stages. During stages 1 and 2, gas molecules are absorbed on one side and diffuse in the material, while in stages 3 and 4, the gas molecules diffuse through the material and are desorbed at the opposite surface [51]. The gas transport through the films is controlled by the diffusivity of gas molecules, which depends on the size of gas molecules, the degree of crystallinity, the porosity and tortuosity of the films, and the aspect ratio of the nanoparticles [52,53]. The rate-limiting step is the diffusion through the film, which strongly depends on the free volume, crystallinity, and porosity of the polymer and the mobility of polymer chains.

CNFs and PVA demonstrated good barrier properties to O_2 at an RH lower than 60 %. On the one hand, the barrier properties of PVA are due to the strong interaction between PVA chains through hydrogen bonds and to the high crystallinity of PVA with a hydrolysis degree over 95 %. On the other hand, for NC, the barrier effect against O_2 resulted from the contribution of different effects: (i) strong interactions between CNFs via hydrogen bonding along with their high aspect ratio, (ii) the ability to form densely packed layers of CNFs, and (iii) the semicrystalline nature of CNFs acting as a barrier against gas permeation. These effects contributed to increasing the tortuosity and diffusion path length for gas molecules, hence reducing gas permeation through the film.

Three reasons may account for the significant evolution of the O_2 permeability of the composite PVC/CNF films: (i) CNFs hindered the crystallization of PVA. Indeed, as demonstrated from the DSC analysis, the crystallization of PVA was inhibited over a critical CNF content (50 wt% T-CNFs and 30 wt% P-CNFs). Due to the higher free volume and lower packing density of amorphous PVA, the permeation of gas molecules was notably favored. (ii) Residual microparticles generated pores facilitating the permeation of O_2 molecules. Between 5 and 10 wt% of partially fibrillated fibers were present in both T-CNFs and P-CNFs, with a lower fraction in P-CNFs. (iii) PVA chains intercalated between CNFs and reduced the cohesion of the layered CNF microstructure.

We infer that the sharp evolution of the OTR over a critical CNF content resulted from the contribution of the lower crystallinity of PVA and the presence of fragments of partially fibrillated fibers. The first hypothesis was supported by the correlation between the sharp increase in the

OTR and the loss of PVA crystallinity. The better performance of P-CNFs is likely due to hemiacetal bonds between CNFs and PVA by condensation between the hydroxyl groups of PVA with the surface aldehyde groups of CNFs.

Our barrier property results differ from those reported by Nuruddin et al. for PVA/CNC composites, where the addition of CNCs to PVA yielded films with the same barrier property to CO_2/O_2 as neat PVA over a 30-90 wt% CNC content [20]. However, in this work, commercial CNCs prepared by H_2SO_4 hydrolysis were used, and the film was prepared by a single-edge razor blade to induce shear-orientation of CNCs.

The evolution of the WVTR value at 23 °C and 50 % RH as a function of CNF content is shown in **Fig. 11B**. The same tendency as for OTR was observed for WVRT, with a sharp increase in water permeability over 50 wt% CNFs. However, the magnitude of the increase was much lower for PVA/P-CNF films, which further illustrates the better barrier properties in the presence of P-CNFs, thanks to the reactive character of the P-CNFs induced by the presence of aldehyde groups.

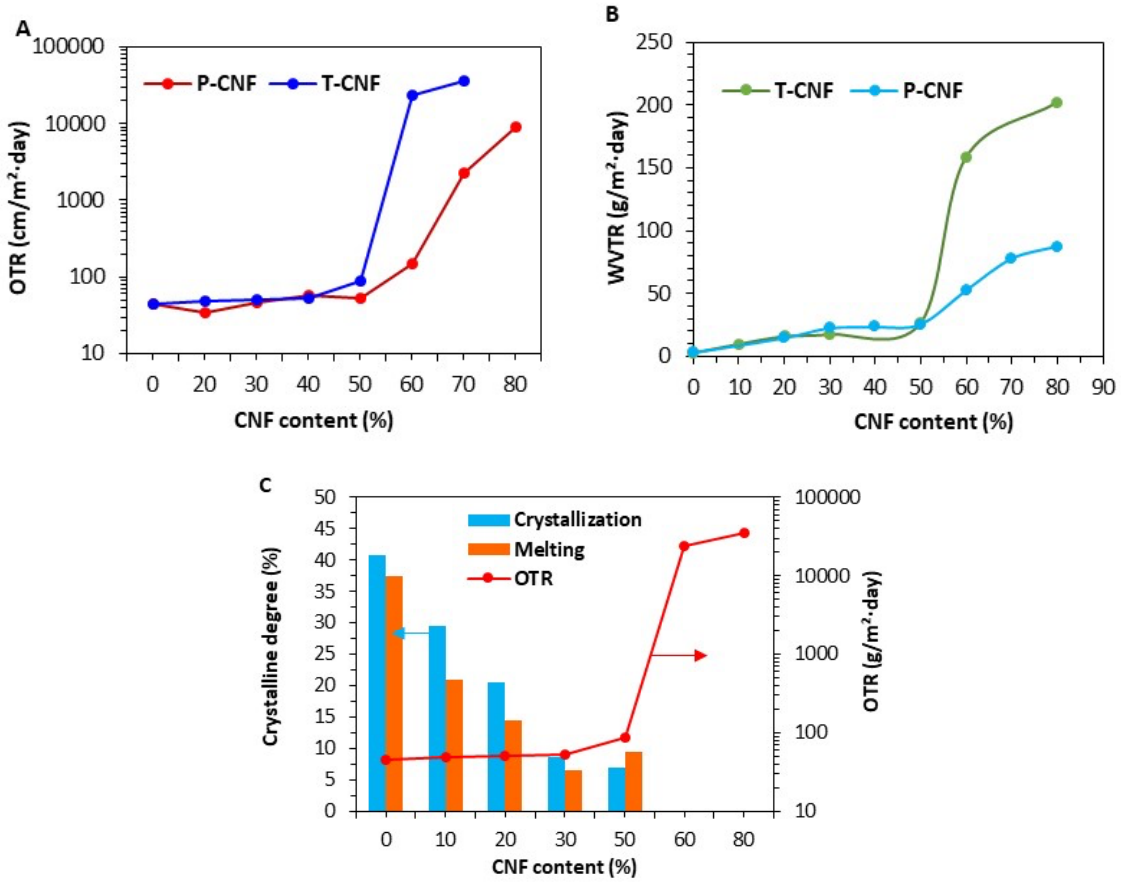

Fig. 11. (A,B) OTR and WVTR at 23 °C and 50 % RH of PVA/CNF films at different CNF contents for T-CNFs and P-CNFs; (C) superposition of the crystalline degree calculated from the melting and crystallization transition in the DSC thermograms,) and OTR for PVA/T-CNF.

However, the magnitude of the increase was much lower for PVA/P-CNF films, which further illustrates the better barrier properties in the presence of P CNFs, thanks to the reactive character of P-CNFs imparted by the aldehyde groups. Moreover, the morphological difference between P-CNFs and T-CNFs may contribute to the different barrier properties in the presence of P-CNFs. Indeed, the higher fibrillation and rodlike shape of P-CNFs would contribute to a better packing of the nanofiller within the PVA matrix and reduce the generation of pores due to the presence of microfragments in the CNF fraction.

4. Conclusion

The mechanical, thermal, optical, and barrier properties of PVA composite films containing two types of CNFs prepared by TEMPO-mediated or periodate oxidation were analyzed. The film exhibited a typical layered structure with good compatibility between PVA and CNFs, favored by the setup of hydrogen bonds between both constituents. The results highlight the efficacy of CNFs to reinforce PVA and improve its thermal stability. The tensile strength and Young's modulus of the composite film significantly increased with increasing CNF content, while the elongation at break decreased. DSC results showed that the crystallization of PVA was inhibited above 50 wt% T-CNFs and 30 wt% P-CNFs. The barrier of PVA/CNF films to water and O_2 was influenced by crystallinity, fibril morphology, and a post-pressure treatment. Furthermore, PVA/T-CNF films without pressure treatment did not exhibit barrier properties. Even without pressing, PVA/P-CNF films exhibited barrier properties, which were attributed to the fact that P-CNFs were much shorter than T-CNFs, resulting in a greater tortuosity of the films. These results can find application in packaging with the coating of papers or biobased polymers by PVA/CNF mixtures to improve barrier properties.

While CNF/PVA composites have previously been reported, most studies have focused on formulations with low CNF content, limiting the exploration of their full potential. The novelty of our work lies in the successful incorporation of high concentrations of CNF into the PVA matrix, a challenging task that requires maintaining the mechanical integrity and flexibility of the material. Moreover, our approach utilized CNFs produced at a high concentration with significantly reduced energy consumption, aligning with sustainable processing principles.

The improved performance of PVA/CNF composite films is due to the complementary properties of the constituents and their strong interfacial interactions, including hydrogen bonding and likely covalent crosslinking. The incorporation of T-CNFs and P-CNFs considerably improved mechanical strength by forming a percolated network, and the compatibility between PVA and CNFs ensured homogeneous dispersion. Notably, no embrittlement of the films was observed, even at high CNF contents, indicating that the PVA/CNF system retained balanced

flexibility and mechanical strength. The resulting materials are suitable for a variety of applications. Their antimicrobial properties via the incorporation of functional additives improved mechanical properties, and barrier to moisture or gases could make them suitable for use in biomedical fields, particularly the PVA/P-CNF formulation, since the potential of cellulose dialdehyde has already been explored in this area. In addition, composites can be used for environmental remediation (e.g., water purification), and their recycling potential and low environmental impact make them ideal for widespread use in industries aiming for more sustainable production and disposal practices.

From an economic standpoint, using a PVA/CNF mixture at an optimal proportion that provides a high barrier performance could facilitate the adoption of paper-based packaging and biodegradable plastic films with enhanced barrier properties. By applying a PVA/CNF suspension coating of appropriate thickness on paper or plastic films, it may be possible to meet the required standards for OTR and WTR. However, further work is needed to optimize the coating process on both paper and plastic films.

Acknowledgements

The authors acknowledge Partenariat Hubert Curien (CMCU project: 23G1118), LabEx Tec 21 (Investissements d'Avenir #ANR-11-LABX-0030), as well as the PHC Utique 23G1118 and the Glyco@Alps program (Investissements d'Avenir #ANR-15-IDEX-02) for financial support. We thank the NanoBio-ICMG Platform (UAR 2607, Grenoble) for granting access to the Electron Microscopy facility, Christine Lancelon-Pin (CERMAV) for the SEM observations, the analytical chemistry platform of UFR Chemistry and Biology (UGA, Grenoble) for providing facilities, and Philippe Le Pellec for technical assistance. CERMAV and LRP are part of Institut Carnot PolyNat (Investissements d'Avenir #ANR-11-CARN-030-01).

CRediT authorship contribution statement

Khadija Trigui: Writing Original Draft, Formal Analysis, Investigation, Writing, Review and Editing. **Albert Magnin:** Writing, Review & Editing, Project administration, Funding acquisition. **Jean-Luc Putaux:** Investigation, Writing, Review & Editing. **Sami Boufi:** Supervision, Project Administration, Funding acquisition, Conceptualization, Writing, Review & Editing.

Declaration of competing interest

The authors declare that they have no known competing financial interests or personal relationships that could have appeared to influence the work reported in this paper.

Data availability

Data will be made available on reasonable request.

References

[1] Li F, Mascheroni E, Piergiovanni L. The Potential of Nanocellulose in the Packaging Field: A Review. Packaging Technology Science 2015;28(6):475–508.

[2] Ahankari SS, Subhedar AR, Bhadauria SS, Dufresne A. Nanocellulose in food packaging: A review. Carbohydrate Polymers 2021;255:117479.

[3] Sobhiga G, J. Maria HJ, Mozetič,, M, Thomas S. A review on green materials: Exploring the potential of poly(vinyl alcohol) (PVA) and nanocellulose composites. International Journal of Biological Macromolecules 2024;283:137176.

[4] Goodship V, Jacobs, D. Polyvinyl Alcohol: Materials, Processing and Application. 2009, Smithers Rapra Technology, Shawbury, Shrewsbury, Shropshire, U.K.

[5] Jain P, Varshney S, Srivastava S. Synthetically modified nano-cellulose for the removal of chromium: a green nanotech perspective. IET Nanobiotechnology 2017;11(1):45–51.

[6] Khoramabadi HN, Arefian M, Hojjati M, Tajzad I, Mokhtarzade A, Mazhar M, Jamavari, A. A review of polyvinyl alcohol / carboxymethyl cellulose (PVA/CMC) composites for various applications. Journal of Composites and Compounds 2020;2(3):69–76.

[7] Lee WJ, Clancy AJ, Kontturi E, Bismarck A, Shaffer MS. Strong and stiff-: High-performance cellulose nanocrystal/poly(vinyl alcohol) composite fibers. ACS Applied Materials & Interfaces 2016;8(46):31500–31504.

[8] Silvério HA, Flauzino Neto WP, Pasquini D. Effect of incorporating cellulose nanocrystals from corncob on the tensile, thermal and barrier properties of poly(vinyl alcohol) nanocomposites. Journal of Nanomaterials, 2013, 289641.

[9] Sirviö J., Honkaniemi S, Visanko M, Liimatainen H. Composite films of poly(vinyl alcohol) and bifunctional cross-linking cellulose nanocrystals. ACS Applied Materials & Interfaces 2045;7(35):19691–19699.

[10] Xu S, Jiang M, Lu Q, Gao S, Feng J, Wang X, He X, Chen K, Li Y, Ouyang P. Properties of polyvinyl alcohol films composited with hemicellulose and nanocellulose extracted from *Artemisia selengensis* straw. Frontiers in Bioengineering and Biotechnology 2020;8, 980.

[11] Leitner J, Hinterstoisser B, Wastyn M, Keckes J, Gindl W. Sugar beet cellulose nanofibril-reinforced composites. Cellulose 2007;14(5):419–425.

[12] Liu D, Sun X, Tian H, Maiti S, Ma Z. Effects of cellulose nanofibrils on the structure and properties on PVA nanocomposites. Cellulose 2013;20(6):2981–2989.

[13] Qiu K, Netravali AN. Fabrication and characterization of biodegradable composites based on microfibrillated cellulose and polyvinyl alcohol. Composites Science and Technology 2012;72(13):1588–1594.

[14] Wu Y, Tang Q, Yang F, Xu, L, Wang X, Zhang J. Mechanical and thermal properties of rice straw cellulose nanofibrils-enhanced polyvinyl alcohol films using freezing-and-thawing cycle method. Cellulose 2019;26(5):3193–3204.

[15] Lu J, Wang T, Drzal LT. Preparation and properties of microfibrillated cellulose polyvinyl alcohol composite materials. Composites Part A: Applied Science and Manufacturing 2008;39(5):738–746.

[16] Li L, Wang W, Sun J, Chen Z, Ma Q, Ke H, Yang J. Improved properties of polyvinyl alcohol films blended with aligned nanocellulose particles induced by a magnetic field. Food Packaging and Shelf Life 2022;34:100985.

[17] Wang Z, Qiao X, Sun K. Rice straw cellulose nanofibrils reinforced poly(vinyl alcohol) composite films. Carbohydrate Polymers 2018;197:442–450.

[18] Liu Y, Chen Y, Qi H. Recyclable cellulose nanofibers reinforced poly (vinyl alcohol) films with high mechanical strength and water resistance. Carbohydrate Polymers 2022;293:119729.

[19] Kim M, Lim T, Park H, Baek KY, Jeong Y, Sohn D, Cho KY, Cho S. Nanocellulose-based optical and radio frequency transparent barrier coating for food packaging. Cellulose 2024;31:5185–5197.

[20] Nuruddin M, Chowdhury RA., Szeto R, Howarter J A, Erk K A, Szczepanski CR, Youngblood JP. Structure–property relationship of cellulose nanocrystal–polyvinyl alcohol thin films for high barrier coating applications. ACS Applied Materials & Interfaces 2021;13(10):12472-12482.

[21] Trigui K, Magnin A, Putaux JL, Boufi S. Twin-screw extrusion for the production of nanocellulose-PVA gels with a high solid content. Carbohydrate Polymers 2022;286:119308.

[22] Trigui, K, De Loubens, C, Magnin, A, Putaux, J-L, Boufi, S. Cellulose nanofibrils prepared by twin-screw extrusion-: Effect of the fiber pretreatment on the fibrillation efficiency. Carbohydrate Polymers 2020;240:116342.

[23] Besbes I, Rei Vilar M, Boufi S. Nanofibrillated cellulose from alfa, eucalyptus and pine fibres: preparation, characteristics and reinforcing potential. Carbohydrate Polymers 2011;86:1198–1206.

[24] Errokh A, Magnin A, Putaux J-L, Boufi S. Morphology of the nanocellulose produced by periodate oxidation and reductive treatment of cellulose fibers. Cellulose 2018;25:3899–3911.

[25] Henriksson M, Berglund LA, Isaksson P, Lindström T, Nishino T. Cellulose Nanopaper Structures of High Toughness. Biomacromolecules 2008;9(6):1579–1585.

[26] Benítez AJ, Torres-Rendon J, Poutanen M, Walther A. Humidity and Multiscale Structure Govern Mechanical Properties and Deformation Modes in Films of Native Cellulose Nanofibrils. Biomacromolecules 2013;14(12):4497–4506.

[27] Pan Y, Liu L, Song L, Hu Y, Jiang S, Zhao H. Reinforcement of layer-by-layer self-assembly coating modified cellulose nanofibers to reduce the flammability of polyvinyl alcohol. Cellulose 2019;26(5):3183–3192.

[28] Yuwawech K, Wootthikanokkhan J, Tanpichai S. Effects of two different cellulose nanofiber types on properties of poly(vinyl alcohol) composite films. Journal of Nanomaterials 2015;2015:908689.

[29] Popescu MC. Structure and sorption properties of CNC reinforced PVA films. International Journal of Biological Macromolecules 2017;101:783–790.

[30] French AD (2014). Idealized powder diffraction patterns for cellulose polymorphs. Cellulose 2014;21(2):885–896

[31] Coates J. Interpretation of infrared spectra, a practical approach. Encyclopedia of Analytical Chemistry 2000;12:10815–10837.

[32] Jia Y, Asoh T-A, Hsu Y-I, Uyama H. Wet strength improvement of starch-based blend films by formation of acetal/hemiacetal bonding. Polymer Degradation and Stability 2020;177:109197.

[33] Asad M, Saba N, Asiri AM, Jawaid M, Indarti E, Wanrosli W D. Preparation and characterization of nanocomposite films from oil palm pulp nanocellulose/poly(vinyl alcohol) by casting method. Carbohydrate Polymers 2018;191:103–111.

[34] Voronova MI, Surov OV, Guseinov S, Barannikov VP, Zakharov A G. Thermal stability of polyvinyl alcohol/nanocrystalline cellulose composites. Carbohydrate Polymers 2015;130:440–447.

[35] Aouay M, Magnin A, Putaux JL, Boufi S. Biobased nucleation agents for poly-L-(lactic acid) - Effect on crystallization, rheological and mechanical properties. International Journal of Biological Macromolecules 2022;218:588–600.

[36] Wang W, Yu Z., Alsammarraie FK, Kong F, Lin M, Mustapha A. Properties and antimicrobial activity of polyvinyl alcohol-modified bacterial nanocellulose packaging films incorporated with silver nanoparticles. Food Hydrocolloids 2020;100:105411.

[37] Cataldi A, Rigotti D, Nguyen V D H, Pegoretti A. Polyvinyl alcohol reinforced with crystalline nanocellulose for 3D printing application. Materials Today Communications 2018;15:236–244.

[38] Deng Q, Li J, Yang J, Li D. Optical and flexible --chitin nanofibers reinforced poly(vinyl alcohol) (PVA) composite film-: Fabrication and property. Composites Part A: Applied Science and Manufacturing 2014;67:55–60.

[39] Virtanen S, Vartianen J, Setälä H, Tammelin T, Vuoti S. Modified nanofibrillated cellulose–polyvinyl alcohol films with improved mechanical performance. RSC Advances 2014;4(22):11343.

[40] Affdl JCH, Kardos JL. The Halpin-Tsai equations: A review. Polymer Engineering and Science 19761;6(5):344-352.

[41] Wu YP, Jia, QX, Yu, DS, Zhang LQ. Modeling Young's modulus of rubber– clay nanocomposites using composite theories. Polymer Testing 2004;23(8):903–909.

[42] Ouali N, Cavaillé JY, Perez J. Elastic, viscoelastic and plastic behavior of multiphase polymer blends. Plastics, Rubber and Composites Processing and Applications 1991;16(1):55–60.

[43] Takayanagi M, Uemura S, Minami S. Application of equivalent model method to dynamic rheo-optical properties of crystalline polymer. Journal of Polymer Science Part C: Polymer Symposia 1964;5(1):113–122.

[44] Azizi Samir MA., Alloin F, Dufresne A. Review of Recent Research into Cellulosic Whiskers, Their Properties and Their Application in Nanocomposite Field. Biomacromolecules 2005;6(2):612–626.

[45] Zhai L, Kim HC, Kim JW, Kang J, Kim J. Elastic moduli of cellulose nanofibers isolated from various cellulose resources by using aqueous counter collision. Cellulose 2018;25:4261–4268.

[46] Favier V, Canova G R, Cavaillé JY, Chanzy H, Dufresne A, Gauthier C. Nanocomposite materials from latex and cellulose whiskers. Polymers for Advanced Technologies 1995;6(5):351–355.

[47] Favier V, Cavaillé JY, Canova GR, Shrivastava S C. Mechanical percolation in cellulose whisker nanocomposites. Polymer Engineering & Science 1997;37(10):1732–1739.

[48] Boufi S, Kaddami H, Dufresne A. Mechanical performance and transparency of nanocellulose reinforced polymer nanocomposites. Macromolecular Materials and Engineering 2014;299:560−568.

[49] Fu S. Effects of fiber length and fiber orientation distributions on the tensile strength of short-fiber-reinforced polymers. Composites Science and Technology 1996;56(10):1179–1190.

[50] Selke SEM, Culter JD, Hernandez RJ, Plastics Packaging; Properties, Processing, Applications and Regulations. Hanser Gardener Publishers, Munich (2004).

[51] Wu Y, Liang Y, Mei C, Cai L, Nadda A, Le QV, Peng Y. Lam SS, Sonne C, Xia C. Advanced nanocellulose-based gas barrier materials-: Present status and prospects. Chemosphere 2022;286:131891.

[52] Hubbe MA, Ferrer A, Tyagi P, Yin Y, Salas C, Pal L, Rojas OJ. Nanocellulose in Thin Films, Coatings, and Plies for Packaging Applications: A Review. BioResources 2017;12(1):2143–2233.

[53] Yampolskii YP, Korikov AP, Shantarovich V, Nagai K, Freeman BD, Masuda T, Teraguchi M, Kwak G. Gas permeability and free volume of highly branched substituted acetylene polymers. Macromolecules 2001;34(6):1788–1796.

Supplementary material

Figure S1. Photos of the (A) twin screw extruder used for the extrusion of the PVA/Fibers mixture, and (B) aspect of the extruded product at the exit of the dye.

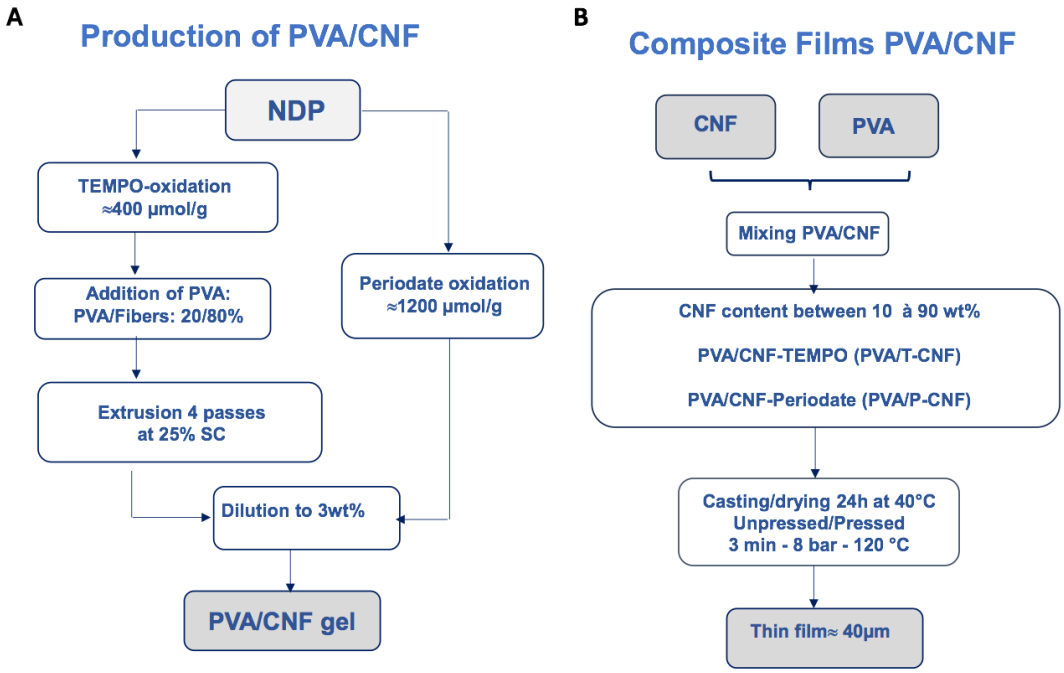

Figure S2: (A) Processing sequence for the production of PVA/CNF gel from T-CNFs and P-CNFs, and (B) preparation route of PVA/CNF composites.

Table S1: Fibrillation degree and turbidity of PVA/T-CNF and PVA/P-CNF composites.

Sample	Turbidity (NTU)	Fibrillation degree (wt%)
PVA/T-CNF	32.0 ± 5.0	90 ± 2
PVA/P-CNF	22.4 ± 5.0	96 ± 2

Figure S3: Optical micrograph of an aqueous suspension of neat cellulose fibers.

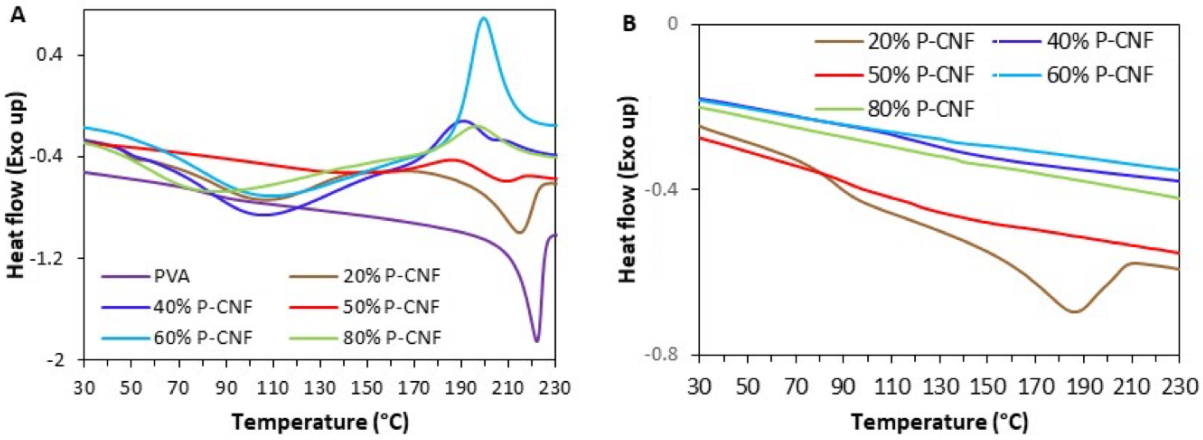

Figure S4: DSC thermograms of PVA/P-CNF films with different CNF contents: (A) first heating; (B) second heating cycle.

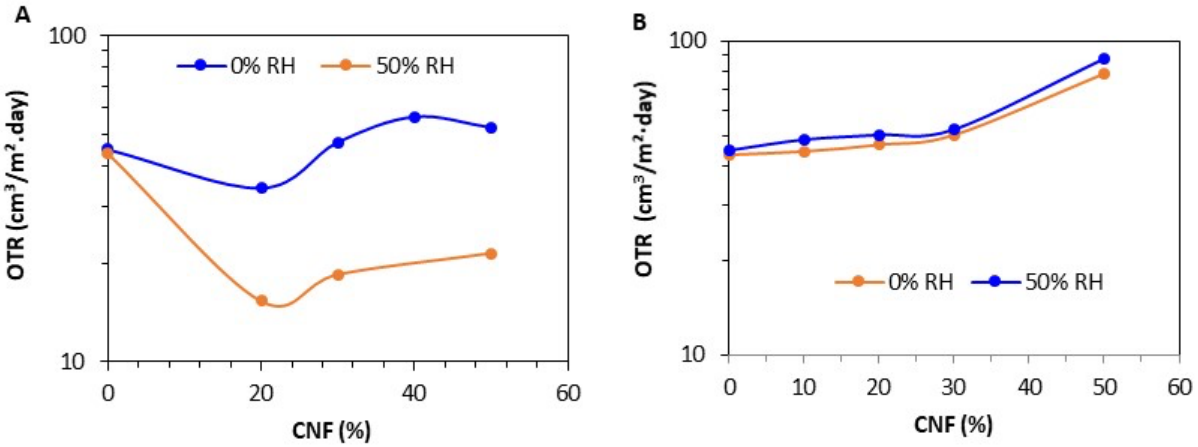

Figure S5: Changes in the OTR of PVA/CNF films at different CNF contents and 50 % RH for T-CNFs (A) and P-CNFs (B).

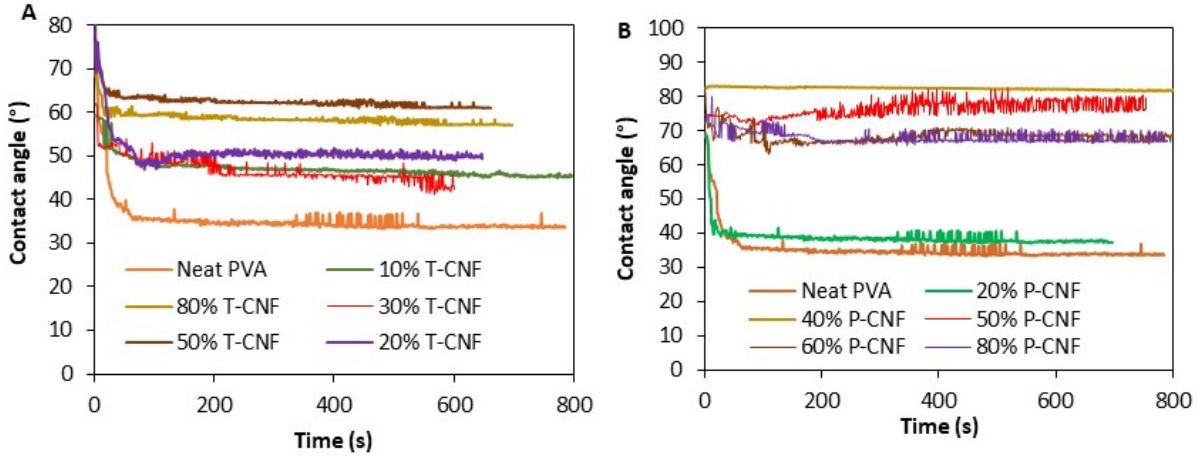

Figure S6. Contact angle as a function of time for a water droplet deposited on PVA/T-CNF (A) and PVA/P-CNF (B) films